

Electronic properties of graphene nanoribbons under gate electric fields

Tobias Burnus,¹ Gustav Bihlmayer,¹ Daniel Wortmann,¹ Yuriy Mokrousov,¹ Stefan Blügel,¹ and Klaus Michael Indlekofer²

¹*Peter Grünberg Institut and Institute for Advanced Simulation, Forschungszentrum Jülich, and Jülich Aachen Research Alliance, 52425 Jülich, Germany*

²*Hochschule RheinMain, Am Brückweg 26, 65428 Rüsselsheim, Germany*

(Dated: November 22, 2021)

Quantum-dot states in graphene nanoribbons (GNR) were calculated using density-functional theory, considering the effect of the electric field of gate electrodes. The field is parallel to the GNR plane and was generated by an inhomogeneous charge sheet placed atop the ribbon. Varying the electric field allowed to observe the development of the GNR states and the formation of localized, quantum-dot-like states in the band gap. The calculation has been performed for armchair GNRs and for armchair ribbons with a zigzag section. For the armchair GNR a static dielectric constant of $\epsilon \approx 4$ could be determined.

PACS numbers: 73.22.Pr, 85.35.Be, 71.15.Ap, 71.15.Mb

I. INTRODUCTION

After their experimental realization, single and bilayer graphene sheets and nanoribbons have attracted intensive attention due to their peculiar properties, which make graphene and its derivatives one of the most prominent material classes for future nanoelectronics.^{1–3} The vast range of possible applications is due to the high carrier mobility,^{4–7} and remarkably long spin lifetimes and phase coherence lengths, which are particularly valuable for quantum information processing.⁸ The peculiar electronic structure of gapless semiconductor graphene prevents electrostatic confinement due to Klein tunneling and gives rise to unique transport properties.⁹ Experimentally, graphene-based tunable nanodevices can be realized, as shown, e.g., for graphene nanoribbons,^{10–12} interference devices,^{13,14} and graphene quantum dots.^{15,16} Graphene nanoribbons (GNRs) play a particularly important role since they are often used in field-effect transistors (FET) setups where the current flow is regulated by a gate electric field. Additionally, gated nanoribbons can also be used to create quantum dots. Hereby, the spin qubits in quantum dots are a promising candidate for quantum information processing,¹⁷ for which graphene is better suited than III–IV semiconductors due to its reduced hyperfine coupling and spin-orbit interaction.^{8,18–22} For nanoelectronics applications, the preferred width of a GNR is in the range of 1–3 nm as for wider ribbons the band gap diminishes.^{23,24}

For a proper theoretical description of GNR FET and GNR-based quantum dots, both the effect of an external electric field and the precise electronic structures of the ribbons have to be considered. In ribbons of small width the details of the termination and exact structure of the edges play an important role for ribbon's electronic structure due to the quantum confinement effects, which have to be properly taken into account. The two most common types of edge termination of the ribbons lead to very different electronic structures in the vicinity of the Fermi energy: while armchair ribbons are insu-

lating with a band gap of up to approximately 2.5 eV, zigzag ribbons exhibit metallic edge states.^{25,26} For the former, the band gap decreases with increasing width of the ribbon and oscillates in magnitude with a periodicity of three as more rows of carbon atoms are added.²³ Experimentally, armchair ribbons with the width of 1 nm with well-defined edges²⁷ and FET with widths down to 2 nm have been realized.²⁸ On the other hand, ribbons with the width of around 50 nm have been used to create quantum dots.^{16,29}

The sensitivity of the electronic properties of narrow GNRs to an external electric field and to the details of the structure, as well as the mechanism for the formation of the quantum dot states, calls for a description and analysis within the highly accurate density-functional theory techniques (DFT). In this work, we study the properties of narrow GNRs in an electric field, generated by finite gates, by employing a new scheme specifically designed for this purpose and realized within the full-potential linearized augmented plane-wave (FLAPW) method. In contrast to common approaches, the latter scheme allows to consider any given distribution of charge in the gates, thus enabling the versatility necessary for studies of complex nanostructured devices from first principles. Here, we describe the details of this approach as implemented within the FLAPW method,³⁰ and study the development of the electronic structure and screening properties of narrow GNRs as the strength of the electric field is varied. We focus particularly on the emergence of the quantum-dot like states, localized under the gates, and analyze their spatial distribution and symmetry properties.

II. INCLUSION OF THE ELECTRIC FIELD

In a realistic device the electronic properties of the graphene nanoribbon will be modified by gate electrodes. While more complex interactions between the gates and the graphene nanoribbon exist, the most prominent ef-

fect of the gates is the electric field they generate. These electric-field effects can be included in a calculation based on DFT,^{31–33} and in the past several different implementations of external fields in DFT codes have been reported.^{34–40} However, in contrast to most of these approaches, which model a situation in which the electric field is applied normally to a surface, the key effect of the gates we study is the field and potential distribution in the plane of the graphene ribbon.

A. Computational scheme

We use the film FLAPW method³⁰ as implemented in the FLEUR code⁴¹ for our calculations. Two slightly different schemes to include the electric fields of the gates have been tested in which the effect of the gates is modeled by: (i) a charged sheet far in the vacuum in which the charge varies parallel to the GNR or (ii) a plane in the vacuum at which a varying boundary condition to the Coulomb potential is applied. While the second approach is closer to the picture of a metallic gate applying an electric field, the generation of the potential from a charge distribution is performed in all existing DFT codes and, hence, the first approach is easy to implement. We discuss all details of the implementation of the gate electric field in the appendix.

For modeling the effect of a gate electrode on a GNR we have chosen a free-standing 13-carbon-atom-wide graphene nanoribbon of armchair type [see Fig. 1(a)]. The dangling bonds are passivated using hydrogen leading to a ribbon which is about 5.1 nm long and 1.7 nm wide, consisting of 312 carbon and 48 hydrogen atoms. The setup is periodically repeated in x -direction to form an infinite ribbon. As our code requires a two-dimensional periodicity, we also have to repeat the ribbon in y direction. A supercell approach with a separation of 5 Å between adjacent cells is used to simulate a single isolated GNR. The center of the GNR is sandwiched between positively charged top and back gates whose charge is compensated by negatively charged top and back gates such that both the GNR and the two charge sheets remain as a whole charge neutral. The positively charged gate has a size of $25.6 \times 12.3 \text{ Å}^2$ and the distance between the GNR plane and the charge sheets is 7 Å. For simplicity, we used a homogeneous surface-charge-density distribution on the gates [method (i)]. However, for the dimensions of this system, the potential at the position of the plane of the GNR is qualitatively the same for a gate with constant potential – the potential only differs strongly close to the gate (not shown). The calculations were performed with the Perdew-Burke-Ernzerhof (PBE) exchange-correlation functional.⁴²

B. Screening of the electrical field

The height dependence (z dependence) of the electric field is shown in Fig. 1(b), cutting vertically through the GNR (with y being at the middle of the ribbon). In the plane of the ribbon ($z = 0$), the field is fully in plane and parallel to the x direction. Above the plane ($|z| > 0$), an out-of-plane component exists, which grows towards the center ($x = 2.55 \text{ Å}$) and the left/right side ($x = 0$ and $x = 5.1 \text{ Å}$). At exactly those points, the field is perpendicular to the GNR plane and the field strength is low, while for the points in between the field is nearly in-plane and stronger. Thus, the potential should cause a charge accumulation under the gate.

Figure 2(a) shows the gate potential along the center of the ribbon for a gate charge of $0.0016e/\text{nm}^2$. These curves have been obtained by subtracting the total potential without an applied field from the potential with applied gate field canceling the potential from the mostly inert ion cores. The (in-plane) applied electric field at the position of the ribbon is given by the slope of the solid black curve and has a maximal value of 0.056 eV/Å . The initial potential due to the applied electric field (black solid curve) gets reduced (red dashed curve) due to the screening by the electrons in the ribbon. This screening effect is determined by evaluating the potential of the self-consistent calculation. From the reduction – the blue dotted curve has been obtained by multiplying the red dashed curve by 3.8 to match the black solid curve – a static ($\omega = 0$) dielectric constant $\epsilon \approx 3.8$ can be deduced for the center of the ribbon. As the calculation has periodic boundary conditions (in x -direction) this static dielectric constant $\epsilon(q)$ corresponds to a wavevector of $q_0 = 0.123 \text{ Å}^{-1}$. The value of $\epsilon(q_0, \omega = 0) \approx 3.8$ agrees with the GW results of Ref. 43. One should note, that the static dielectric constant has been evaluated in the linear response limit of a small electric field, for stronger fields and especially close to the crossover of states [cf. Fig. 4(b)], different values are obtained.⁴⁴

The dependence of the screening on the distance from the GNR plane is shown in Fig. 2(b); ϵ reduces only slightly from 3.8 to 3.4 over 1 Å. This relatively constant screening corresponds to presence of charge density due to the p_z orbitals, which is still significant at these distances. For larger distances to the GNR ϵ decreases exponentially, approaching the vacuum value of 1.

III. RESULTS

A. Straight armchair ribbon

In this section, we focus on the formation of quantum dot states in an armchair GNR with a width of 13 carbon atoms by applying an electric field as outlined in the previous section. The edges of the ribbon are hydrogen-terminated and it is placed between the electrodes as

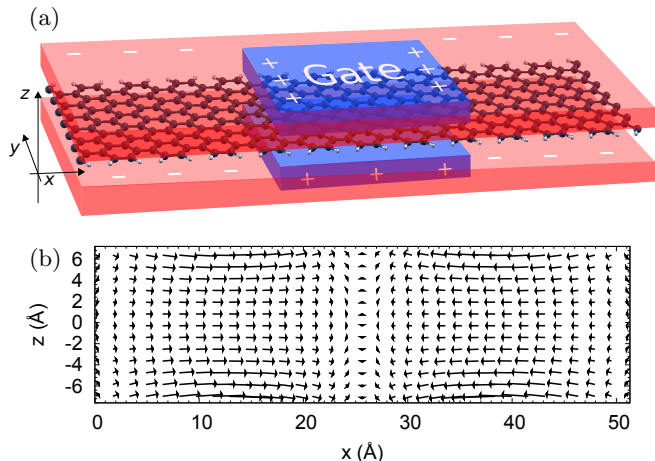


FIG. 1. (Color online) (a) Free-standing, hydrogen-terminated armchair graphene nanoribbon of 13 atoms width. The blue rectangles indicate the location of the positively charged top and bottom gate electrodes. Their charge is compensated by the negatively charged top and bottom electrodes (shown in red). (b) Side view showing the electric field created by the electrodes (for y at the middle of the ribbon).

visualized in Fig. 1(a). If one compares the total electron density of this structure without field and with a field of 0.67 V/\AA (this corresponds to a charge of $\pm 0.19e/\text{nm}^2$ on the gates), the charge accumulation and depletion can be visualized by a density-difference plot as shown in Fig. 3. Predominately charge of the p_z orbitals is localized under the positively charged gate forming a “quantum dot” of about 20 \AA diameter.

To investigate the effect of the electric field on the electronic structure of the GNR, we first consider in Fig. 4(a) the bandstructure of the ribbon without field. The bandgap is about 0.9 eV and bounded by valence and conduction band states at the Γ point. Introducing an additional periodicity in x -direction by the field leads to a backfolding of the bandstructure along Γ - X . If the field is modulated with a periodicity of 51 \AA (12 unit cells in x -direction), the backfolding occurs at the red lines shown in Fig. 4(a). The Brillouin zone extends then from Γ to X' . In the following we focus on the states at the Γ point, since they form the valence and conduction band edge.

Switching on the electric field leads to a splitting or a shift of the eigenenergies as shown in Fig. 4(b): The two-fold degeneracy of the states at -0.75 eV and $+0.7 \text{ eV}$, which results from the backfolding of the Brillouin zone, is lifted and the bands split almost symmetrically, both for negative and positive fields. The slight asymmetry between positive and negative electric field is introduced by the shape of the gate electrode as shown in Fig. 1(a). If there were just a one-dimensionally modulated field acting on the GNR, this asymmetry would vanish. The splitting can then be understood from the consideration of a system with just two eigenstates

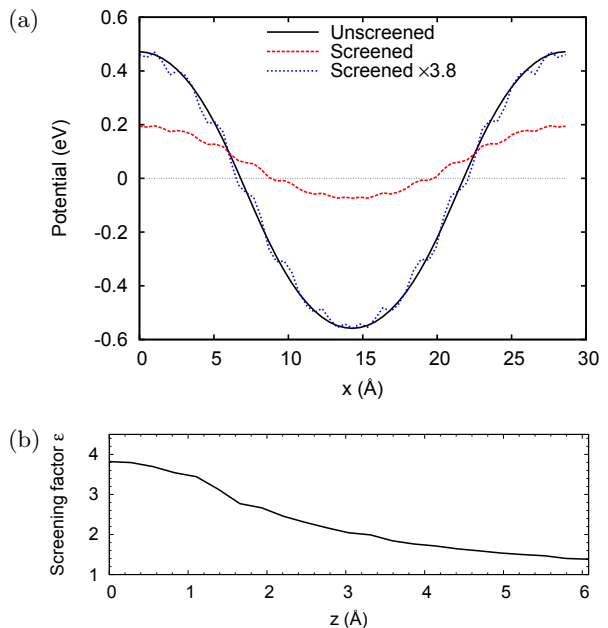


FIG. 2. (Color online) (a) Potential due to the gate electric field along center of the GNR ($z = 0$). The black solid curve shows the applied gate potential, the red dashed curve the screened potential. The blue dotted curve is obtained by multiplying the red dashed curve by 3.8, indicating a static dielectric constant of $\epsilon \approx 3.8$. (b) Dependence of the static screening on the distance from the plane.

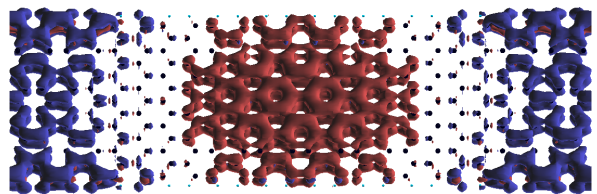


FIG. 3. (Color online) Total charge density difference between a calculation with gate electric field and without; the density is reduced (blue) at outside and increased (red) in the center.

with energies ϵ_0^+ and ϵ_0^- , perturbed by a periodic potential with Fourier coefficients V_i . At the i^{th} backfolding of the bandstructure, the states split according to $\epsilon_{1,2}(V) = \frac{1}{2}(\epsilon_0^+ + \epsilon_0^-) \pm \sqrt{\frac{1}{4}(\epsilon_0^+ - \epsilon_0^-)^2 + |V_i|^2}$. As the states are degenerate, the splitting is linear in $|V_i|$. In case of interacting states that are non-degenerate, the evolution of these states starts parabolic at small fields and evolves into a more linear behavior at stronger fields ($V_i \gg (\epsilon_0^+ - \epsilon_0^-)$).

With increasing field strength the uppermost valence band states move up in energy, towards the Fermi level, while the lowest conduction band states move down by a similar amount. Their interaction causes again a deviation from the linear behavior and at a field strength corresponding to 0.4 V/\AA the first crossover of states oc-

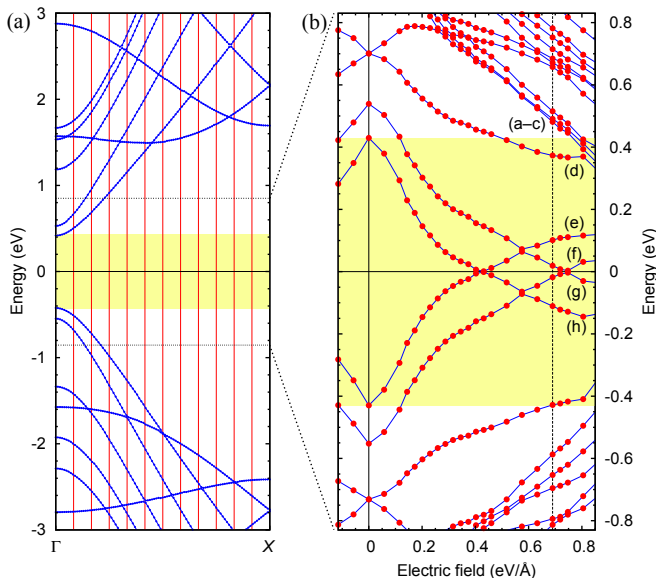


FIG. 4. (Color online) (a) Band structure for the smallest, 13 carbon atom wide GNR ($1/12$ as long as the gated GNR) with four staggered carbon atom in x direction and totally 26 carbon atoms; the zero-field band gap of about 0.9 eV is shaded in yellow. (b) Single-particle eigenenergies gated GNR for the Γ point in dependence of the applied electric field. The energy is relative to the Fermi energy; the abscissa shows maximal electric field (gradient of the potential before screening) at position of the ribbon. The states at the dashed vertical line [(a)–(h)] are depicted in Fig. 5.

curs, i.e. a valence band state becomes unoccupied while a conduction band state is populated. In order to get a better understanding of this scenario, we display the single-particle states in this energy region in Fig. 5 for a field of 0.67 eV/\AA [vertical line in Fig. 4(b)]. The first crossover occurs for states shown in Fig. 5(e) and (h), i.e. with state (h) the first quantum dot state gets localized under the gate electrode. State (e) has more density outside the positively gated region; it raises in energy with increasing field and gets unoccupied.

At stronger fields (0.72 eV/\AA) the state Fig. 5(f) gets occupied, which can be regarded as the second quantum dot state. As for atoms, one expects also for quantum dots states an increasing number of nodal planes for higher states with higher energy, which is indeed what one observes: The color of the isosurfaces in Fig. 5 denotes the sign of the wavefunction, which allows to locate the nodal planes. The first quantum-dot state (h) has at the center one vertical nodal plane (dashed green line) and is not nodeless as one might have expected. For the next localized state (f) one sees in the charge density a horizontal nodal plane, while the state (c) has two: a horizontal and a vertical nodal plane. The state (b) seems to have two horizontal and the state (a) one horizontal and two vertical nodal planes.

We have thus shown how under a gate electric field, localized states appear in the band gap; those show a

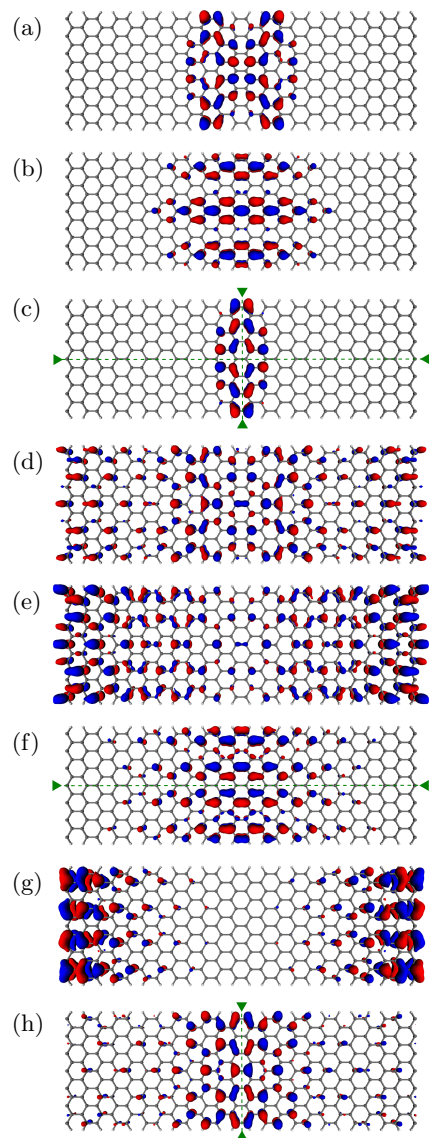


FIG. 5. (Color online) Charge density of the single-particle levels at a field of 0.67 eV/\AA , ordered descending in energy; (a)–(f) are above, (g) and (h) below the Fermi energy. The color of the isosurfaces denotes the sign of the wavefunction.

nodal structure as one expects for a quantum dot. The states still show the structure of the underlying lattice and are predominately formed by p_z states as one can see in the charge density.

B. Z-shaped ribbon

Besides armchair nanoribbons, also zigzag ribbons exist, which are known for their (conducting) edge states.^{25,26,45} Those are located just above and below the Fermi energy. The combination of both types of edge states could be useful for future nanodevices; but missing atoms or sections with different edge terminations

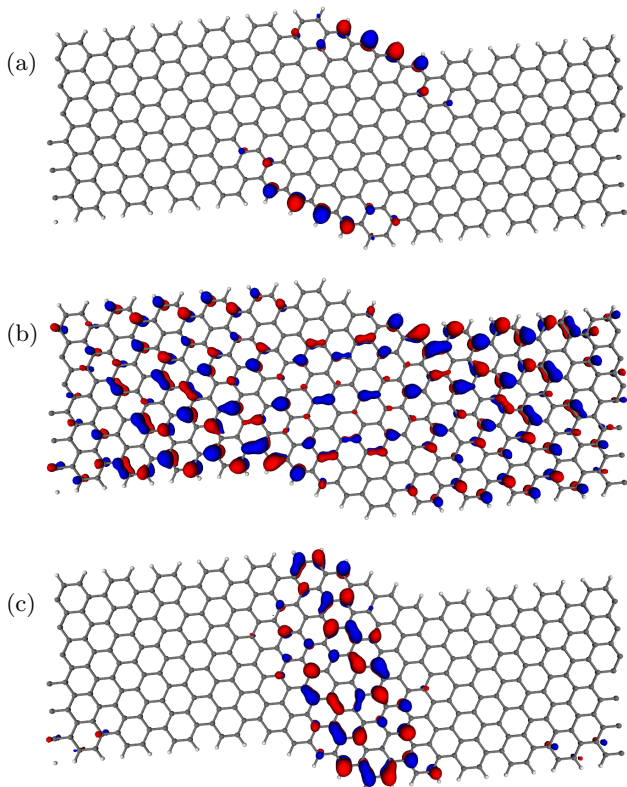


FIG. 6. (Color online) Armchair nanoribbon with zigzag section. (a) Edge state at the Fermi energy (no field). (b) State above 0.87 eV above the Fermi energy (no field). (c): Same state with an applied gate field of 1 eV/Å, now located at the Fermi energy.

might also occur involuntarily during the preparation of nanoribbons. We have thus simulated an armchair ribbon of width 13 (as above) but with a zigzag section in the middle.

For the calculation, a supercell with length of 51.3 Å and width of 25.8 Å has been used; the positive gate charge has been placed at the center over and below the zigzag region ($16 \times 18.8 \text{ Å}^2$). Figure 6(a) shows (for zero field) the existence of an edge state in the zigzag section; the highest occupied (shown) and the lowest unoccupied state have the same density but locally different phases. If one now turns on an electric field, the edge states gain density in the middle of the ribbon. Additionally, states with more density at the outside raise in energy, while more localized states get more localized and become lower in energy. This is exemplified in Fig. 6 for an electric field of 1 eV/Å (maximal potential gradient before screening; gate charge is $0.026e/\text{nm}^2$): (b) shows a high lying state at zero field (0.87 eV above the Fermi energy), which moves down in energy to the Fermi energy in the electric field; at the same time its density becomes more localized at the zigzag region, i.e. under the gate.

IV. CONCLUSION

A scheme to include arbitrary electrical fields has been introduced and its implementation for the film FLAPW method outlined. The scheme allows for Neumann and Dirichlet boundary conditions and for differently shaped gate electrodes. Future use could encompass the calculation of the effects of an electrical field on adatom on films and a wide range other electric-field related phenomena.

The gate electric field was then applied to an armchair graphene nanoribbon; the mostly in-plane field caused a charge accumulation under the gate. For small fields, the linear response of the electrons in the ribbon to the electric field allowed to determine a static dielectric constant of $\epsilon = 3.8$. The field also drove states into the zero-field gap; as has been shown, the previously unoccupied states entering the gap region are localized under the gate. Those states, mostly formed by p_z orbitals, show the structure of the underlying lattice. However, they also feature a nodal structure as one would expect for quantum dots. The states have been obtained from an all-electron density-functional theory calculation, which makes a comparison to less precise techniques such as tight binding interesting; those techniques have the advantage that much larger systems can be treated. Additionally, the influence of the electric field on GNR consisting of zigzag with metallic edge states and semiconducting armchair sections has been shown, where the electric field moves states towards the Fermi energy, which are localized under the gate.

ACKNOWLEDGMENTS

The calculations were performed on the Juropa supercomputer at the Forschungszentrum Jülich, Germany. The work was supported by Deutsche Forschungsgemeinschaft through Research Unit 912 “Coherence and Relaxation Properties of Electron Spins”. Y. M. acknowledges funding under the HGF-YIG programme VH-NG-513.

Appendix A: Electric field in FLAPW

For periodic systems, the full-potential linearized augmented plane wave (FLAPW) basis, used for the calculations presented above, gives an accurate, all-electron description.^{30,46–51} Besides the more common FLAPW basis with three-dimensional periodicity, a film version of FLAPW exists. It has only two-dimensional periodicity and semi-infinite vacua in the third direction (chosen to be z).^{30,49,50,52,53} Hereby, the space is separated into three regions: the muffin-tin spheres around each atom, the interstitial region between the spheres and a vacuum region in which the density decays exponentially to zero; see Fig. 7. The basis set used for expansion of the wavefunction consists of the functions of the following form:

$$\varphi_{\mathbf{G}_{\parallel}G_{\perp}}(\mathbf{k}_{\parallel}, \mathbf{r}) = \begin{cases} e^{i(\mathbf{G}_{\parallel} + \mathbf{k}_{\parallel})\mathbf{r}} e^{iG_{\perp}z}, & \text{interstitial} \\ [a_{\mathbf{G}_{\parallel}, G_{\perp}}(\mathbf{k}_{\parallel})u_{\mathbf{G}_{\parallel}}(\mathbf{k}_{\parallel}, z) + b_{\mathbf{G}_{\parallel}, G_{\perp}}(\mathbf{k}_{\parallel})\dot{u}_{\mathbf{G}_{\parallel}}(\mathbf{k}_{\parallel}, z)]e^{i(\mathbf{G}_{\parallel} + \mathbf{k}_{\parallel})\mathbf{r}} & \text{vacuum} \\ \sum_L [a_L^{\mu\mathbf{G}}(\mathbf{k})u_L(r) + b_L^{\mu\mathbf{G}}(\mathbf{k})\dot{u}_L(r)]Y_L(\hat{\mathbf{r}}) & \mu\text{-th muffin tin} \end{cases}, \quad (\text{A1})$$

where $\mathbf{G} = \mathbf{G}_{\parallel} + (0, 0, G_{\perp})$ is the reciprocal lattice vector, the u_L are radial functions with \dot{u}_L as their energy derivatives, Y_L are spherical harmonics, $\hat{\mathbf{r}} = \mathbf{r}/|\mathbf{r}|$, and a and b are coefficients chosen such that the basis function is continuously differentiable across the interstitial–vacuum and interstitial–muffin-tin boundary. The \parallel denotes the in-plane (x – y) and \perp the out-of-plane (z) component. While the interstitial extends to $|z| \leq z_1 \equiv D_{\text{vac}}/2$, the perpendicular wavevectors G_{\perp} are defined with regard to $\bar{D} > D_{\text{vac}}$, i.e. $G_{\perp} = 2\pi n/\bar{D}$, to allow for more variational freedom.

1. Neumann boundary conditions

The idea is to obtain the potential by integrating the surface charge density σ from infinity, i.e.

$$V(\mathbf{r}) = -\frac{1}{\varepsilon_0} \int_{-\infty}^z \sigma(\mathbf{r}') dz', \quad (\text{A2})$$

with $d\sigma/dz = \rho$, where ρ is the charge density. The complication in evaluating the equation (A2) arises from the use of different bases in the different regions. The electric field \mathcal{E} could be included in the calculation via its associated potential V_{EF} as an additional term to the external potential V_{ext} ; however, in the presented scheme it enters as charge density ρ_{EF} . Their relation is given by $\varepsilon_0 \nabla^2 V_{\text{EF}} = \varepsilon_0 \nabla \cdot \mathcal{E} = -\rho_{\text{EF}}$, where ε_0 is the electric constant (for cgs replace ε_0 by $1/4\pi$).

For the vacuum region, the charge ρ and the potential V can be expanded in a Fourier series,^{37,38,40}

$$V(\mathbf{r}) = \sum_{\mathbf{G}_{\parallel}} V_{\mathbf{G}_{\parallel}}(z) e^{i\mathbf{G}_{\parallel}\mathbf{r}}, \quad \rho(\mathbf{r}) = \sum_{\mathbf{G}_{\parallel}} \rho_{\mathbf{G}_{\parallel}}(z) e^{i\mathbf{G}_{\parallel}\mathbf{r}}; \quad (\text{A3})$$

thus, the Laplace operator of the Poisson equation $\varepsilon_0 \nabla^2 V = -\rho$ separates into a z and \mathbf{G}_{\parallel} term,

$$\varepsilon_0 \left[\frac{\partial^2}{\partial z^2} - \mathbf{G}_{\parallel}^2 \right] V_{\mathbf{G}_{\parallel}}(z) = -\rho_{\mathbf{G}_{\parallel}}(z), \quad (\text{A4})$$

which leads to two equations. For $\mathbf{G}_{\parallel} = 0$ (uniform field in the vacuum), Eq. (A4) can be solved by integration. Using the boundary condition that the potential smoothly vanishes at infinity, $\lim_{z \rightarrow \infty} V(z) = 0$ and $\lim_{z' \rightarrow \infty} \partial_z V(z)|_{z'} = 0$, the potential in the vacuum is given by

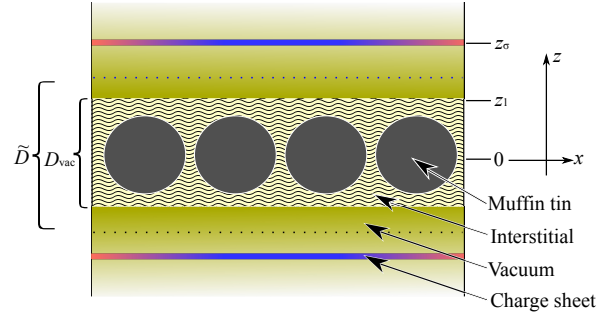


FIG. 7. (Color online) Geometric setup in the FLAPW method with muffin-tin spheres, interstitial, and two semi-infinite vacuum regions in z direction. $|z| = z_1 \equiv D_{\text{vac}}/2$ marks the interstitial–vacuum boundaries, $|z_{\sigma}|$ is the position for the charge sheets.

$$\begin{aligned} V_{\mathbf{G}_{\parallel}=0}(z) &= -\frac{1}{\varepsilon_0} \int_z^{\infty} \int_{z'}^{\infty} \rho(z'') dz'' dz' \\ &= \frac{1}{\varepsilon_0} \int_z^{\infty} (z' - z) \rho(z'') dz'. \end{aligned} \quad (\text{A5})$$

For the nonuniform part, $\mathbf{G}_{\parallel} \neq 0$, the Green function

$$G(z, z') = \frac{1}{2|\mathbf{G}_{\parallel}|} e^{-|\mathbf{G}_{\parallel}| \cdot |z - z'|} \quad (\text{A6})$$

can be used to give a particular solution for the potential,

$$V_{\mathbf{G}_{\parallel}}(z) = \frac{1}{\varepsilon_0} \int_{z_0}^z G(z, z') \rho_{\mathbf{G}_{\parallel}}(z') dz', \quad (\text{A7})$$

which fulfills the boundary condition that the potential vanishes for $z_0 \rightarrow \infty$ smoothly at infinity.

If the system has no mirror symmetry, e.g. because the field on the top is different from the one at the bottom, the charge density can be written as^{37,54}

$$\rho^{(1)}(z) = \begin{cases} \rho_0(z) + \bar{\rho} + \sum_{\mathbf{G} \neq 0} \rho_{\mathbf{G}} e^{i\mathbf{G}\cdot\mathbf{r}}, & |z| \leq z_1 \\ 0, & |z| > z_1 \end{cases} \quad (\text{A8})$$

$$\rho^{(2)}(z) = \begin{cases} -\bar{\rho}, & |z| \leq z_1 \\ \rho_0(z) + \sum_{\mathbf{G} \neq 0} \rho_{\mathbf{G}} e^{i\mathbf{G}\cdot\mathbf{r}}, & |z| > z_1 \end{cases} \quad (\text{A9})$$

where $-\bar{\rho}$ denotes the average pseudo charge density of the interstitial, i.e.

$$\begin{aligned}\bar{\rho} &= \frac{1}{2z_1} \int_{-z_1}^{z_1} \rho_{\mathbf{G}_{\parallel}=0}(z) dz \\ &= -\rho_{0,0} - \sum_{G_{\perp} \neq 0} \rho_{0,G_{\perp}} j_0(G_{\perp} z_1),\end{aligned}\quad (\text{A10})$$

with $\rho_{\mathbf{G}_{\parallel}=0}(z) = \sum_{G_{\perp}} \rho_{0,G_{\perp}} \exp(iG_{\perp} z)$ and Bessel function $j_0(z) = \sin z/z$. To obtain the potential, one sums up the surface charge densities starting from minus infinity; the electric field is included as surface charge density σ_{EF} . For the vacuum region, the $\mathbf{G}_{\parallel} = 0$ component of the potential is given by

$$\begin{aligned}V(z < -z_1) &= -\frac{1}{\varepsilon_0} \int_{-\infty}^z \sigma(z') dz' \\ &\quad -\theta(z - z_{\sigma}^{(-)}) \frac{1}{\varepsilon_0} \int_{z_{\sigma}^{(-)}}^z \sigma_{\text{EF}}^{(-)} dz' \\ V(z > z_1) &= -\frac{1}{\varepsilon_0} \int_{z_1}^z [\sigma(z') + (-\bar{\rho})D_{\text{vac}} + \sigma(-z_1)] dz' \\ &\quad -\theta(z - z_{\sigma}^{(+)}) \frac{1}{\varepsilon_0} \int_{z_{\sigma}^{(+)}}^z \sigma_{\text{EF}}^{(+)} dz' \\ &\quad +V_{z_1} + \phi\end{aligned}\quad (\text{A11})$$

$$\sigma(z < -z_1) = \int_{-\infty}^z \rho(z') dz'$$

$$\sigma(z > z_1) = \int_{z_1}^z \rho(z') dz \quad (\text{A12})$$

where V_{z_1} is the potential at z_1 and ϕ is a phase due to the dipole moment, which is only present if the system has neither mirror nor inversion symmetry. The potential is given by

$$\begin{aligned}V_{z_1} &= V(-z_1) + \frac{1}{\varepsilon_0} (\sigma(-z_1)D_{\text{vac}} + \frac{1}{2}D_{\text{vac}}^2(-\bar{\rho})) \\ \phi &= -\frac{1}{\varepsilon_0} \sum_{G_{\perp} \neq 0} \int_{-z_1}^{z_1} z \rho_{0,G_{\perp}} e^{iG_{\perp} z} dz \\ &= -\frac{2i}{\varepsilon_0} \sum_{G_{\perp} \neq 0} j_1(G_{\perp} z_1) \rho_{0,G_{\perp}} z_1^2,\end{aligned}\quad (\text{A13})$$

where $j_1(z) = (\sin z - z \cos z)/z^2$.

For the $\mathbf{G}_{\parallel} \neq 0$ component the solution is given by Eq. (A7); for the FLAPW basis, the integration has to be split into two vacua and the film region; for a given $z > |z_1|$ the integral in the vacuum can be further split into $\int_{z_1}^z$ and $\int_z^{z_{\sigma}}$, which has been done to obtain the functions α and β below; the vacuum potential is then given by

$$\begin{aligned}V_{\mathbf{G}_{\parallel}}(\pm|z|) &= -\frac{1}{2\varepsilon_0|\mathbf{G}_{\parallel}|} \left[e^{\mathbf{G}_{\parallel}|z|} \alpha_{\mathbf{G}_{\parallel}}(\mp|z|) \right. \\ &\quad \left. + e^{-|\mathbf{G}_{\parallel}||z|} \beta_{\mathbf{G}_{\parallel}}(\mp|z|) \right. \\ &\quad \left. + e^{-|\mathbf{G}_{\parallel}||z|} \alpha_{\mathbf{G}_{\parallel}}(\pm|z|) \right]\end{aligned}\quad (\text{A14})$$

with

$$\alpha_{\mathbf{G}_{\parallel}}(\pm|z|) = \pm \int_{\pm z}^{\pm\infty} \tilde{\rho}_{\mathbf{G}_{\parallel}}(z') e^{-|\mathbf{G}_{\parallel}||z'|} dz' \quad (\text{A15})$$

$$\beta_{\mathbf{G}_{\parallel}}(\pm|z|) = \pm \int_{\pm z_1}^z \tilde{\rho}_{\mathbf{G}_{\parallel}}(z') e^{|\mathbf{G}_{\parallel}||z'|} dz', \quad (\text{A16})$$

where $\tilde{\rho}_{\mathbf{G}_{\parallel}}(z) = \rho_{\mathbf{G}_{\parallel}}(z) + \delta(|z| - z_{\sigma}) \sigma_{\text{EF},\mathbf{G}_{\parallel}}^{(\text{sgn } z)}$ and $\sigma_{\text{EF},\mathbf{G}_{\parallel}}^{(\text{sgn } z)}$ is the (inhomogeneous) surface charge density of, respectively, the top and bottom charge sheet.

2. Dirichlet boundary conditions

Contrary to the Neumann boundary condition used above, which defines the boundary via a surface charge density, the Dirichlet boundary condition has a fixed potential at the boundaries, which matches metallic plates held a certain voltage. The Dirichlet boundary conditions not only imply a different single-particle potential but due to the density-dependent image charges the effective Coulomb interaction between electrons is modified.^{55,56} The effect of the latter is not included in the described scheme and would require a modified functional.

For the constant-potential boundary condition, the $\mathbf{G}_{\parallel} = 0$ part, solved by integrating Eq. (A4), is given by

$$\begin{aligned}V_0(z) &= -\frac{1}{\varepsilon_0} \int_{z_0}^z \int_{z_0}^{z'} \rho_0(z'') dz'' dz' \\ &\quad + \frac{1}{\varepsilon_0} (z - z_0) \sigma_0 + V_0 \\ &= -\frac{1}{\varepsilon_0} \int_{z_0}^z \sigma(z') dz' + \frac{1}{\varepsilon_0} (z - z_0) \sigma_0 + V_0,\end{aligned}\quad (\text{A17})$$

with $\sigma(z) = \int_{z_0}^z \rho(z') dz'$. The lower boundary is set to $-z_{\sigma}$, the location of the metallic plate with the associated potential $V_0 = V_{-z_{\sigma}}$. For the other plate at $+z_{\sigma}$, the potential $V_{z_{\sigma}}$ is given by

$$V_0(z_{\sigma}) = -\frac{1}{\varepsilon_0} \int_{-z_{\sigma}}^{z_{\sigma}} \sigma(z') dz' + 2z_{\sigma} \frac{\sigma_0}{\varepsilon_0} + V_0; \quad (\text{A18})$$

thus,

$$\frac{\sigma_0}{\varepsilon_0} = \frac{1}{2z_{\sigma}} \left[V_{z_{\sigma}} - V_{-z_{\sigma}} + \frac{1}{\varepsilon_0} \int_{-z_{\sigma}}^{z_{\sigma}} \sigma(z') dz' \right] \quad (\text{A19})$$

which can be used in a similar way to the Neumann solution described above.

To solve the Poisson equation for $\mathbf{G}_{\parallel} \neq 0$, we start with the solution of the homogeneous problem $[\partial_z^2 - \mathbf{G}_{\parallel}^2] V_{\mathbf{G}_{\parallel}}(z) = 0$, which is given by

$$\tilde{V}_{\mathbf{G}_{\parallel}}(z) = C_1 e^{-|\mathbf{G}_{\parallel}|z} + C_2 e^{+|\mathbf{G}_{\parallel}|z}. \quad (\text{A20})$$

The coefficients C_1 and C_2 have to be chosen such that the boundary condition $V_{\mathbf{G}_{\parallel}}(-z_{\sigma}) = V_{-z_{\sigma}}^{(\mathbf{G}_{\parallel})}$ and $V_{\mathbf{G}_{\parallel}}(z_{\sigma}) = V_{z_{\sigma}}^{(\mathbf{G}_{\parallel})}$ are fulfilled; one obtains

$$C_1 = \frac{V_{-z_{\sigma}}^{(\mathbf{G}_{\parallel})} x - V_{z_{\sigma}}^{(\mathbf{G}_{\parallel})} y}{x^2 - y^2}, C_2 = \frac{V_{z_{\sigma}}^{(\mathbf{G}_{\parallel})} x - V_{-z_{\sigma}}^{(\mathbf{G}_{\parallel})} y}{x^2 - y^2}; \quad (\text{A21})$$

hereby $x = \exp(|\mathbf{G}_{\parallel}|z_{\sigma})$ and $y = \exp(-|\mathbf{G}_{\parallel}|z_{\sigma})$. On the other hand, a Green's function solving Eq. (A4) is given by⁵⁵

$$G(z, z') = \frac{1}{|\mathbf{G}_{\parallel}| \sinh(\mathbf{G}_{\parallel} 2z_{\sigma})} \times \begin{cases} \sinh \mathbf{G}_{\parallel}(z_{\sigma} - z') \sinh \mathbf{G}_{\parallel}(z + z_{\sigma}), & z \leq z' \\ \sinh \mathbf{G}_{\parallel}(z' + z_{\sigma}) \sinh \mathbf{G}_{\parallel}(z_{\sigma} - z), & z > z' \end{cases} \quad (\text{A22})$$

which vanishes at the boundary $\pm z_{\sigma}$; for $z_{\sigma} \rightarrow \infty$ it simplifies to Eq. (A6). Using this Green's function, the particular solution is given by

$$V_{\mathbf{G}_{\parallel}}^{(\text{part})}(z) = \frac{1}{\varepsilon_0} \int G(z, z') \rho_{\mathbf{G}_{\parallel}}(z') dz'. \quad (\text{A23})$$

Combining the regular solution of the homogeneous system with the particular solution gives

$$V_{\mathbf{G}_{\parallel}}(z) = \frac{1}{\varepsilon_0} \int_{-z_{\sigma}}^{z_{\sigma}} \rho_{\mathbf{G}_{\parallel}}(z') G(z, z') dz' + C_1 e^{-|\mathbf{G}_{\parallel}|z} + C_2 e^{+|\mathbf{G}_{\parallel}|z} \quad (\text{A24})$$

with the C_1 and C_2 as defined above.

-
- ¹ A. K. Geim and K. S. Novoselov, "The rise of graphene," *Nature Mater.* **6**, 183 (2007), arXiv:cond-mat/0702595 [cond-mat.mtrl-sci].
- ² A. H. Castro Neto, F. Guinea, N. M. R. Peres, K. S. Novoselov, and A. K. Geim, "The electronic properties of graphene," *Rev. Mod. Phys.* **81**, 109 (2009), arXiv:0709.1163 [cond-mat.other].
- ³ A. K. Geim, "Graphene: Status and prospects," *Science* **324**, 1530 (2009), arXiv:0906.3799 [cond-mat.mes-hall].
- ⁴ K. S. Novoselov, A. K. Geim, S. V. Morozov, D. Jiang, M. I. Katsnelson, I. V. Grigorieva, S. V. Dubonos, and A. A. Firsov, "Two-dimensional gas of massless Dirac fermions in graphene," *Nature (London)* **438**, 197 (2005), arXiv:cond-mat.mes-hall [cond-mat/0509330].
- ⁵ Y. Zhang, Y.-W. Tan, H. L. Stormer, and P. Kim, "Experimental observation of the quantum Hall effect and Berry's phase in graphene," *Nature (London)* **438**, 201 (2005), arXiv:cond-mat/0509355 [cond-mat.mes-hall].
- ⁶ P. Avouris, Z. Chen, and V. Perebeinos, "Carbon-based electronics," *Nat. Nanotechnol.* **2**, 605 (2007).
- ⁷ S. Das Sarma, S. Adam, E. H. Hwang, and E. Rossi, "Electronic transport in two-dimensional graphene," *Rev. Mod. Phys.* **83**, 407 (2011), arXiv:1003.4731 [cond-mat.mes-hall].
- ⁸ B. Trauzettel, D. V. Bulaev, D. Loss, and G. Burkard, "Spin qubits in graphene quantum dots," *Nature Physics* **3**, 192 (2007), arXiv:cond-mat/0611252.
- ⁹ M. I. Katsnelson, K. S. Novoselov, and A. K. Geim, "Chiral tunnelling and the Klein paradox in graphene," *Nature Physics* **2**, 620 (2006), arXiv:cond-mat/0604323 [cond-mat.mes-hall].
- ¹⁰ Z. Chen, Y.-M. Lin, M. J. Rooks, and P. Avouris, "Graphene nano-ribbon electronics," *Physica E* **40**, 228 (2007), arXiv:cond-mat/0701599 [cond-mat.mtrl-sci].
- ¹¹ M. Y. Han, B. Özyilmaz, Y. Zhang, and P. Kim, "Energy band-gap engineering of graphene nanoribbons," *Phys. Rev. Lett.* **98**, 206805 (2007), arXiv:cond-mat/0702511 [cond-mat.mes-hall].
- ¹² X. Li, X. Wang, L. Zhang, S. Lee, and H. Dai, "Chemically derived, ultrasmooth graphene nanoribbon semiconductors," *Science* **319**, 1229 (2008).
- ¹³ F. Miao, S. Wijeratne, Y. Zhang, U. C. Coskun, W. Bao, and C. N. Lau, "Phase-coherent transport in graphene quantum billiards," *Science* **317**, 1530 (2007), arXiv:cond-mat/0703052 [cond-mat.mes-hall].
- ¹⁴ S. Russo, J. B. Oostinga, D. Wehenkel, H. B. Heersche, S. S. Sobhani, L. M. K. Vandersypen, and A. F. Morpurgo, "Observation of Aharonov-Bohm conductance oscillations in a graphene ring," *Phys. Rev. B* **77**, 085413 (2008), arXiv:0711.1508 [cond-mat.mes-hall].
- ¹⁵ C. Stampfer, E. Schurtenberger, F. Molitor, J. Güttinger, T. Ihn, and K. Ensslin, "Tunable graphene single electron transistor," *Nano Lett.* **8**, 23782383 (2008), arXiv:0806.1475 [cond-mat.mes-hall].
- ¹⁶ L. A. Ponomarenko, F. Schedin, M. I. Katsnelson, R. Yang, E. W. Hill, K. S. Novoselov, and A. K. Geim, "Chaotic Dirac billiard in graphene quantum dots," *Science* **320**, 356 (2008), arXiv:0801.0160 [cond-mat.mes-hall].
- ¹⁷ D. Loss and D. P. DiVincenzo, "Quantum computation with quantum dots," *Phys. Rev. A* **57**, 120 (1998), arXiv:cond-mat/9701055 [cond-mat.mes-hall].
- ¹⁸ C. L. Kane and E. J. Mele, "Quantum spin hall ef-

- fect in graphene,” *Phys. Rev. Lett.* **95**, 226801 (2005), arXiv:cond-mat/0411737 [cond-mat.mes-hall].
- ¹⁹ H. Min, J. E. Hill, N. A. Sinitsyn, B. R. Sahu, L. Kleinman, and A. H. MacDonald, “Intrinsic and Rashba spin-orbit interactions in graphene sheets,” *Phys. Rev. B* **74**, 165310 (2006), arXiv:cond-mat/0606504 [cond-mat.mes-hall].
- ²⁰ D. Huertas-Hernando, F. Guinea, and A. Brataas, “Spin-orbit coupling in curved graphene, fullerenes, nanotubes, and nanotube caps,” *Phys. Rev. B* **74**, 155426 (2006), arXiv:cond-mat/0606580 [cond-mat.mes-hall].
- ²¹ C. Stampfer, J. Güttinger, F. Molitor, D. Graf, T. Ihn, and K. Ensslin, “Tunable coulomb blockade in nanostructured graphene,” *Appl. Phys. Lett.* **92**, 012102 (2008), arXiv:0709.3799 [cond-mat.mes-hall].
- ²² X. Liu, J. B. Oostinga, A. F. Morpurgo, and L. M. K. Vandersypen, “Electrostatic confinement of electrons in graphene nanoribbons,” *Phys. Rev. B* **80**, 121407(R) (2009), arXiv:0812.4038 [cond-mat.mes-hall].
- ²³ Y.-W. Son, M. L. Cohen, and S. G. Louie, “Energy gaps in graphene nanoribbons,” *Phys. Rev. Lett.* **97**, 216803 (2006), arXiv:cond-mat/0611602 [cond-mat.mes-hall].
- ²⁴ G. Fiori and G. Iannaccone, “Simulation of graphene nanoribbon field-effect transistors,” *IEEE Electron Device Lett.* **28**, 760 (2007), arXiv:0704.1875 [cond-mat.mes-hall].
- ²⁵ M. Fujita, K. Wakabayashi, K. Nakada, and K. Kusakabe, “Peculiar localized state at zigzag graphite edge,” *J. Phys. Soc. Jpn.* **65**, 1920 (1996).
- ²⁶ Z. F. Wang, Q. W. Shi, Q. Li, X. Wang, J. G. Hou, H. Zheng, Y. Yao, and J. Chen, “Z-shaped graphene nanoribbon quantum dot device,” *Appl. Phys. Lett.* **91**, 053109 (2007), arXiv:0705.0023 [cond-mat.mes-hall].
- ²⁷ J. Cai, P. Ruffieux, R. Jaafar, M. Bieri, T. Braun, S. Blankenburg, M. Muoth, A. P. Seitsonen, M. Saleh, X. Feng, K. Müllen, and R. Fasel, “Atomically precise bottom-up fabrication of graphene nanoribbons,” *Nature (London)* **466**, 470 (2010).
- ²⁸ X. Wang, Y. Ouyang, X. Li, H. Wang, J. Guo, and H. Dai, “Room-temperature all-semiconducting sub-10-nm graphene nanoribbon field-effect transistors,” *Phys. Rev. Lett.* **100**, 206803 (2008), arXiv:0803.3464 [cond-mat.mes-hall].
- ²⁹ J. Güttinger, T. Frey, C. Stampfer, T. Ihn, and K. Ensslin, “Spin states in graphene quantum dots,” *Phys. Rev. Lett.* **105**, 116801 (2010), arXiv:1002.3771 [cond-mat.mes-hall].
- ³⁰ H. Krakauer, M. Posternak, and A. J. Freeman, “Linearized augmented plane-wave method for the electronic band structure of thin films,” *Phys. Rev. B* **19**, 1706 (1979).
- ³¹ P. Hohenberg and W. Kohn, “Inhomogeneous electron gas,” *Phys. Rev.* **136**, B864 (1964).
- ³² W. Kohn and L. J. Sham, “Self-consistent equations including exchange and correlation effects,” *Phys. Rev.* **140**, A1133 (1965).
- ³³ C. Fiolhais, F. Nogueira, and M. A. Marques, eds., *A Primer in Density Functional Theory*, Lecture Notes in Physics, Vol. 620 (Springer, Berlin, 2003).
- ³⁴ L. Bengtsson, “Dipole correction for surface supercell calculations,” *Phys. Rev. B* **59**, 12301 (1999).
- ³⁵ J. Neugebauer and M. Scheffler, “Theory of adsorption and desorption in high electric fields,” *Surf. Sci.* **287-288**, 572 (1993).
- ³⁶ B. Meyer and D. Vanderbilt, “Ab initio study of BaTiO₃ and PbTiO₃ surfaces in external electric fields,” *Phys. Rev. B* **63**, 205426 (2001), arXiv:cond-mat/0009288 [cond-mat.mtrl-sci].
- ³⁷ H. Erschbaumer, *Berechnung der elektronischen Struktur einer Silberelektrode unter Berücksichtigung eines externen Potentials*, Ph.D. thesis, Universität Wien (1988) (in German).
- ³⁸ H. Erschbaumer, R. Podloucky, and A. Neckel, “First-principles simulation of a charged electrode: the electronic structure of a Ag(001) surface under the influence of an external electrostatic field,” *Surf. Sci.* **237**, 291 (1990).
- ³⁹ S. Heinze, X. Nie, S. Blügel, and M. Weinert, “Electric-field-induced changes in scanning tunneling microscopy images of metal surfaces,” *Chem. Phys. Lett.* **315**, 167 (1999).
- ⁴⁰ M. Weinert, G. Schneider, R. Podloucky, and J. Redinger, “FLAPW: applications and implementations,” *J. Phys.: Condens. Matter* **21**, 084201 (2009).
- ⁴¹ FLEUR, <http://www.flapw.de/>.
- ⁴² J. P. Perdew, K. Burke, and M. Ernzerhof, “Generalized gradient approximation made simple,” *Phys. Rev. Lett.* **77**, 3865 (1996).
- ⁴³ M. van Schilfgaarde and M. I. Katsnelson, “First-principles theory of nonlocal screening in graphene,” *Phys. Rev. B* **83**, 081409 (2011), arXiv:1006.2426 [cond-mat.mes-hall].
- ⁴⁴ T. Burnus, G. Bihlmayer, D. Wortmann, Y. Mokrousov, S. Bugel, and K. M. Indlekofer, unpublished.
- ⁴⁵ K. Nakada, M. Fujita, G. Dresselhaus, and M. S. Dresselhaus, “Edge state in graphene ribbons: Nanometer size effect and edge shape dependence,” *Phys. Rev. B* **54**, 17954 (1996).
- ⁴⁶ P. M. Marcus, “Variational methods in the computation of energy bands,” *Int. J. Quantum Chem.* **1**, 567 (1967).
- ⁴⁷ D. D. Koelling and G. O. Arbman, “Use of energy derivative of the radial solution in an augmented plane wave method: application to copper,” *J. Phys. F: Met. Phys.* **5**, 2041 (1975).
- ⁴⁸ O. K. Andersen, “Linear methods in band theory,” *Phys. Rev. B* **12**, 3060 (1975).
- ⁴⁹ E. Wimmer, H. Krakauer, M. Weinert, and A. J. Freeman, “Full-potential self-consistent linearized-augmented-plane-wave method for calculating the electronic structure of molecules and surfaces. . .,” *Phys. Rev. B* **24**, 864 (1981).
- ⁵⁰ M. Weinert, E. Wimmer, and A. J. Freeman, “Total-energy all-electron density functional method for bulk solids and surfaces,” *Phys. Rev. B* **26**, 4571 (1982).
- ⁵¹ D. J. Singh and L. Nordstrom, *Planewaves, Pseudopotentials and the LAPW Method* (Springer, New York, 2006).
- ⁵² S. Blügel and G. Bihlmayer, “The full-potential linearized augmented plane wave method,” in *Computational Nanoscience: Do It Yourself!*, NIC Series, Vol. 31, edited by J. Grotendorst, S. Blügel, and D. Marx (John von Neumann Institute, Jülich, 2006) pp. 85–129 and references therein.
- ⁵³ P. Kurz, *Non-Collinear Magnetism at Surfaces and in Ultrathin Films*, Ph.D. thesis, RWTH Aachen (2000).
- ⁵⁴ M. Weinert, unpublished (1984).
- ⁵⁵ L. D. Hallam, J. Weis, and P. A. Maksym, “Screening of the electron-electron interaction by gate electrodes in semiconductor quantum dots,” *Phys. Rev. B* **53**, 1452 (1996).
- ⁵⁶ K. M. Indlekofer, J. Knoch, and J. Appenzeller, “Quantum kinetic description of coulomb effects in one-dimensional nanoscale transistors,” *Phys. Rev. B* **72**, 125308 (2005), arXiv:cond-mat/0504746 [cond-mat.other].